IEEE Photonics Journal
An IEEE Photonics Society Publication

Open Access

Cascaded Integration of Optical Waveguides With Third-Order Nonlinearity With Lithium Niobate Waveguides on Silicon Substrates

Volume 10, Number 3, JUNE 2018

Amirmahdi Honardoost, *Student Member, IEEE*
Guillermo Fernando Camacho Gonzalez
Saeed Khan
Marcin Malinowski
Ashutosh Rao, *Student Member, IEEE*
Jean-Etienne Tremblay
Anupama Yadav
Kathleen Richardson
Ming C. Wu, *Fellow, IEEE*
Sasan Fathpour, *Senior Member, IEEE*

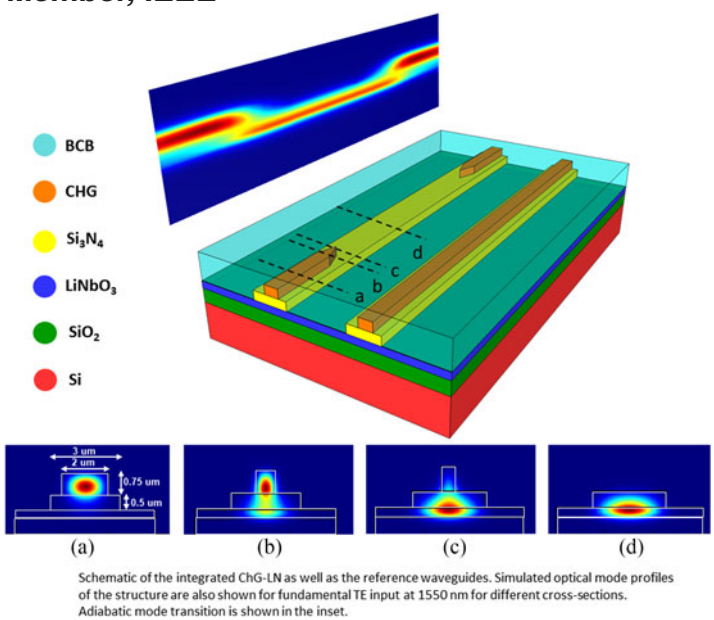

Schematic of the integrated ChG-LN as well as the reference waveguides. Simulated optical mode profiles of the structure are also shown for fundamental TE input at 1550 nm for different cross-sections. Adiabatic mode transition is shown in the inset.

DOI: 10.1109/JPHOT.2018.2827995
1943-0655

IEEE photonics SOCIETY

IEEE

Cascaded Integration of Optical Waveguides With Third-Order Nonlinearity With Lithium Niobate Waveguides on Silicon Substrates

Amirmahdi Honardoost,[1,2] *Student Member, IEEE*, Guillermo Fernando Camacho Gonzalez,[2] Saeed Khan,[1] Marcin Malinowski,[1] Ashutosh Rao,[1] *Student Member, IEEE*, Jean-Etienne Tremblay,[3] Anupama Yadav,[1] Kathleen Richardson,[1] Ming C. Wu,[3] *Fellow, IEEE*, and Sasan Fathpour,[1,2] *Senior Member, IEEE*

[1]CREOL, The College of Optics and Photonics, University of Central Florida, Orlando, FL 32816, USA
[2]Department of Electrical and Computer Engineering, University of Central Florida, Orlando, FL 32816, USA
[3]Department of Electrical Engineering and Computer Sciences, University of California, Berkeley, CA 94720, USA

DOI:10.1109/JPHOT.2018.2827995

Manuscript received January 5, 2018; revised April 9, 2018; accepted April 13, 2018. Date of publication April 17, 2018; date of current version June 19, 2018. This work was supported in part by the Defense Advanced Research Projects Agency under the DODOS project (DARPA-BAA-14-31), in part by the U.S. Office of Naval Research under the project N00014-17-1-2409 and in part by the U.S. Department of Energy (DoE) SBIR program under the project DE-SC0013245. Corresponding author: Sasan Fathpour (e-mail: fathpour@creol.ucf.edu).

Abstract: The cascaded integration of optical waveguides with third-order optical nonlinearity ($\chi^{(3)}$ susceptibilitiy) with lithium niobate ($LiNbO_3$) waveguides is demonstrated on the same chip. Thin-film ($LiNbO_3$) and chalcogenide (ChG) glass ($Ge_{23}Sb_7S_{70}$) waveguides are integrated on silicon (Si) substrates. An optical mode transition between the two waveguides is achieved through low-loss mode-converting tapers, with a measured loss of ~1.5 dB for transverse-electric and ~1.75 dB for transverse-magnetic input polarizations. For nonlinear characterization, wavelength conversion via four-wave mixing is demonstrated on the ChG-LN waveguides. This platform provides an efficient method for the utilization of second- and third-order optical nonlinearities on the same chip, rendering it ideal for nonlinear applications such as stabilized octave-spanning optical frequency comb generation.

Index Terms: Photonic integrated circuits, nanophotonics, nonlinear optics, silicon photonics.

1. Introduction

There has been a dramatic increase of interest in Silicon (Si) photonics since the late 1980s [1]–[3]. Silicon photonics has been widely pursued as a promising technology for a variety of applications such as in datacom transceivers [2]. However, several shortcomings are well-known for Si, when it comes to nonlinear optical applications. For example, Si inherently lacks second-order optical susceptibility ($\chi^{(2)}$) due to its centrosymmetric lattice structure. This restricts convenient utilization

of standard silicon photonics for applications such as second-harmonic generation (SHG). Also, the presences of two-photon and free-carrier absorptions (TPA and FCA), at the required high optical intensities, limit the exploitation of silicon's large third-order optical susceptibility ($\chi^{(3)}$), at least at telecom wavelengths [2], [4].

Several approaches have been pursued in order to circumvent silicon photonics lack of $\chi^{(2)}$-based optical nonlinearity. Heterogeneous integration of other materials on Si with second-order nonlinearity, e.g., lithium niobate (LN) [5], [6], and aluminum nitride (AlN) [7], [8] is one approach. Electric field-induced $\chi^{(2)}$ nonlinearity [9], as well as waveguides stressed under silicon nitride (Si_3N_4 or SiN) [10] are other approaches. A detailed review of all these approaches has been recently published [11]. Similarly, heterogeneous integration of materials with high $\chi^{(3)}$ and insignificant TPA have been pursued to avoid silicons shortcoming for third-order nonlinear integrated optics. Si_3N_4, chalcogenide (ChG) glass, hydrogenated amorphous Si (a-Si:H), and Hydex are some of the major non-organic example materials [4]. Organic materials and hybrid silicon-organic structures have been long pursued as well [12]–[14].

Evidently, there has been several works on integration of other nonlinear materials on silicon. However, the efforts have been primarily limited to integrating a "single" material. Naturally, the new frontline of research should target monolithic integration of "multiple" materials/devices for more advanced functionalities on the same chip. For example, it is very important to "co-integrate" cascaded waveguides with $\chi^{(2)}$ and $\chi^{(3)}$ properties in the context of frequency-stabilized optical comb generation. The $\chi^{(3)}$ waveguide provides octave-spanning supercontinuum generation (SCG), while second-harmonic generation in the $\chi^{(2)}$ device is used for stabilization by f-to-2f carrier-envelope offset (CEO) locking [15], [16]. The present work is the first effort in paving the path towards integration of two example materials, namely ChG ($\chi^{(3)}$) and lithium niobate ($LiNbO_3$, LN) ($\chi^{(2)}$) waveguides, towards this goal.

LN is one of the most widely used materials for nonlinear optical applications. Transparency in a broad range of the electromagnetic spectrum (0.4$-$5 μm), strong second-order nonlinearity, as well as a large electrooptic coefficient [4] make LN an ideal material for integration with Si photonics for applications such as SHG [5], [6], and optical modulation [17], [18] . Potential future demonstrations on silicon may include generation of entangled photon pairs for quantum-optic applications [19], [20]. However, conventional LN devices (fabricated using dopant diffusion [21], or proton-exchange processes [22]) are bulky in general and exhibit low efficiency in terms of power consumption and device footprint, hence hampering the desired large-scale integration capability. Compact LN waveguides, based on bonding of thin films of LN on oxidized Si substrates, have been demonstrated and pursued towards satisfying the requirement of large-scale integration [18]. Moreover, by loading the LN thin films with a rib waveguide made out of a refractive-index-matched material (such as tantalum pentoxide (Ta_2O_5) [18], ChG [23], or Si_3N_4 [17]), high optical confinement and low loss has been achieved. Consequently, these submicron rib-loaded (hybrid) waveguides have rendered themselves useful for compact $\chi^{(2)}$-based nonlinear-optic applications [5], [6], as well as high-performance electrooptic modulation [17], [18], [23]. Coincidentally and as mentioned above, Si_3N_4 and ChG are also among commonly employed materials fabricated on oxidized Si for their strong $\chi^{(3)}$-based nonlinearities [4]. Recently, the heterogeneous integration of Si_3N_4 waveguides with thin-film LN on Si has been demonstrated, but no nonlinear measurement was reported [24]. Moreover, nonlinear refractive index of ChG (3.71×10^{-18} m^2/W) [25] is almost 15 times larger than that of Si_3N_4 (0.24×10^{-18} m^2/W) [26]. These properties combined with the possibility of obtaining high optical confinement and low-loss waveguides make ChG an attractive candidate for various nonlinear applications [25], [27]–[30].

This work reports on cascaded integration of ChG glass and thin-film LN waveguides on the same Si chip. Carefully designed mode-converting tapers are employed for adiabatic optical mode transition from ChG to hybrid LN waveguides and vice versa. In comparison to the previous report on integration of Si_3N_4 waveguides with thin-film LN [24], our proposed platform has the advantages of eliminating the need for LN bonding at the final stages of the processing, and offers a simpler fabrication process. Also, as proof of concept, we provide four-wave mixing (FWM) results on the ChG portion of the ChG-LN integrated devices.

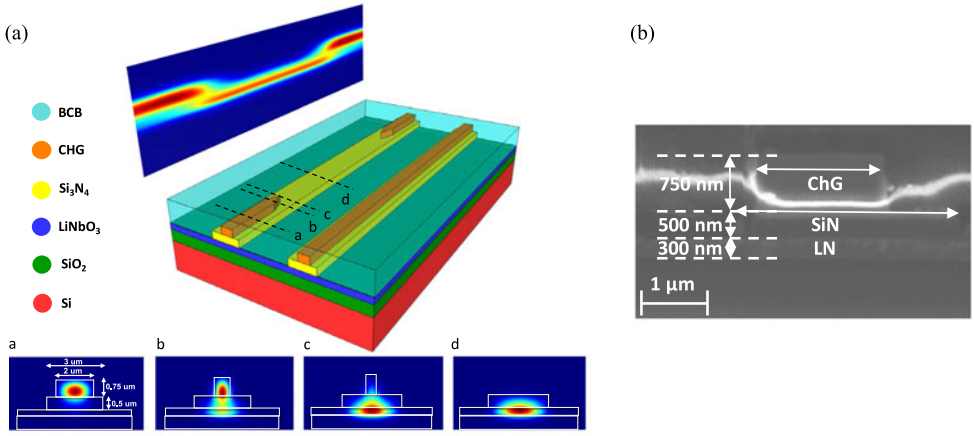

Fig. 1. (a) Schematic of the integrated ChG-LN as well as the reference waveguides. Simulated optical mode profiles of the structure are also shown for fundamental TE input at 1550 nm for different cross-sections. Adiabatic mode transition is shown in the inset. (b) A cross-section SEM image of the fabricated devices at position b of the taper.

2. Design and Simulation

The schematic of the integrated platform is shown in Fig. 1(a). The optical mode profiles of the structure are simulated by using Lumerical Mode Solutions. The fundamental transverse-electric (TE) mode at 1550 nm is shown at different cross-sections of the structure. The input mode is mainly distributed in the ChG rib, due to its higher refractive index compared to Si_3N_4's. By introducing the tapered region, the optical mode gradually transfers into the Si_3N_4-LN lower waveguide, where $\sim$50% of the mode distribution is confined within the LN thin film. The top-left inset depicts the adiabatic TE-mode transition from the upper waveguide region (ChG) to the lower one (Si_3N_4-LN) by the 500-μm length of the taper and vice versa. Adiabatic mode transition for negligible TE-mode coupling loss is found to be occurring at taper lengths of $>$100 μm, according to the Lumerical simulations depicted in Fig. 2(a). Meanwhile, similar simulations show that the coupling efficiency for the transverse-magnetic (TM) input mode is $\sim$90%. This lower coupling efficiency is due to the fact that the TM mode is less confined than the TE mode. This behavioral difference between TE and TM modes in tapers has been observed in other waveguide platforms [31].

It should be stressed that the Si_3N_4 waveguide, between the ChG waveguide and the LN slab, plays an important role. By inserting the lower-index Si_3N_4 layer, $\chi^{(3)}$ and $\chi^{(2)}$ (i.e., ChG and LN) are uncoupled in the untapered regions. In other words, the Si_3N_4 buffer ensures that the LN slab does not interfere with the mode in the ChG waveguide, which is engineered to achieve the desired dispersion.

It is also noted that the present cascaded integration of ChG and/or Si_3N_4 and LN waveguides should not be confused with the aforementioned rib-loading of LN with similar materials for hybrid waveguide formation [5], [6], [17], [18], [23]. In those works, ChG, Si_3N_4 or any other index-matched material is solely used as a rib-loading layer on top of LN thin films for lateral optical confinement in order to avoid the difficulties of etching LN. That is, exploiting the $\chi^{(3)}$ nonlinearity of the rib-loading material is not intended in those works.

Fig. 2(b) shows the simulated coupling efficiency of the tapers versus wavelength, suggesting a large bandwidth for the proposed structure. In addition to the large optical bandwidth, high error tolerance is also predicted by the simulation results. Fig. 2(c) depicts the coupling efficiency of the

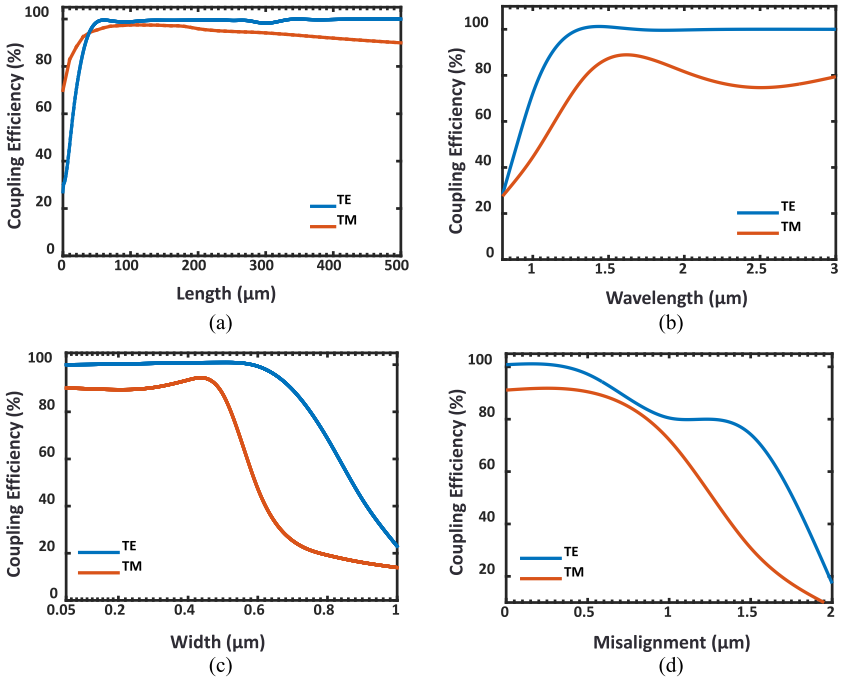

Fig. 2. Simulated coupling efficiency of the mode-converting tapers vs. (a) Length of the taper; (b) Wavelength; (c) Width of the taper's tip; and (d) Misalignment between the centers of the ChG waveguide/taper and Si_3N_4-LN waveguide.

taper versus the width of its tip. Coupling efficiency is also shown versus the misalignment between the centers of the ChG waveguide/taper and the underneath Si_3N_4-LN waveguide in Fig. 2(d).

3. Fabrication

The fabrication process begins with a 300-nm-thick *X*-cut LN thin film wafers from NanoLN. A 500-nm-thick layer of Si_3N_4 was deposited on the LN thin films, using plasma-enhanced chemical vapor deposition (PECVD). The deposition was performed at 750 mTorr pressure and 300 °C temperature, with a gas mixture of 2% silane and nitrogen, flowing at 2000 and 10 sccm, respectively. The 3-μm-wide ribs were patterned using electron-beam lithography (EBL), followed by dry etching using inductively-coupled plasma reactive-ion etching (ICP-RIE). The process parameters of 20 and 5 sccm for flows of CHF_3 and Ar, respectively, biasing power of 70 W, ICP power of 300 W and pressure of 7 mTorr were used. Then, a 750-nm-thick layer of ChG glass, $Ge_{23}Sb_7S_{70}$, was deposited using a thermal evaporator. The ChG glass was patterned and etched to form the waveguides along with the mode-converting tapers, on top of the Si_3N_4 rib waveguides. Same gases and flow rates were used as in the Si_3N_4 etch, but at a lower pressure of 5 mTorr. The biasing and ICP powers were 300 and 100 W, respectively.

The particular glass composition of $Ge_{23}Sb_7S_{70}$ has been used in our previous works and optimized for low-loss waveguides and the required refractive index [28], [29]. The film refractive indices at 1550 nm wavelength were measured to be 2.21, 1.93, and 2.24 for LN, Si_3N_4 and ChG respectively, using the prism-coupling method. The lengths of the two ChG straight sections, shown in Fig. 1(a), are 4.0 mm, each, and the corresponding lengths of the tapered regions are 0.5 mm, each, with a 1-mm Si_3N_4 gap in between. 10-mm-long reference waveguides without tapers were also fabricated on the same chip [as shown in Fig. 1(a)] which are used to isolate the mode transition losses, induced by the tapers. Finally, a 2-μm-thick layer of benzocyclobutene (BCB) was spun and cured on top to serve as a passivation layer, as well as the top cladding for the devices. Fig. 1(b) shows a scanning-electron microscopy (SEM) image of the cross-section of a fabricated waveguide

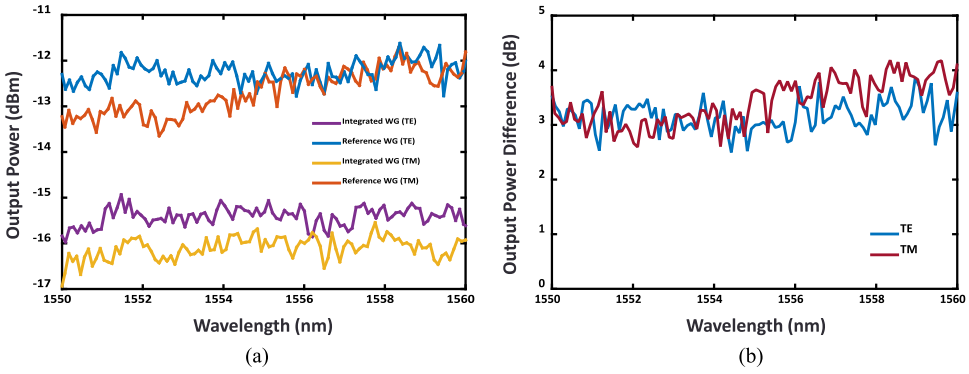

Fig. 3. (a) Optical spectra of output power (10 dBm input power) for the integrated as well as the reference waveguides for both TE and TM input polarizations in the 1550–1560 nm wavelength range; (b) Output power difference between the integrated and reference waveguides for TE and TM input polarizations for the same wavelength range.

with labeled material regions. The lateral asymmetry of the ChG and Si_3N_4 waveguides is due to lithography misalignment. The measured LN, Si_3N_4 and ChG layer thicknesses are in agreement with the targeted values reported in the fabrication steps.

4. Characterization

4.1 Linear Characterization

The devices are characterized by using a tunable single-mode continuous-wave (CW) laser source. The TE output from a polarization controller is end-butt coupled into the waveguides through a lensed fiber. Another lensed fiber couples the light out of the waveguides into a photodetector in order to measure the output optical power and hence the insertion loss. Both the ChG-Si_3N_4-LN integrated devices as well as the reference waveguides (with no tapers) are characterized. The measurements are also done for the TM input polarization. The results are presented in Fig. 3(a) over the wavelength range of 1550–1560 nm for 10 dBm input power. The evident ∼22 dB insertion is mostly attributed to not incorporating optical mode-converters at the chips' input and output facets.

Fig. 3(b) shows the output power difference between the integrated and reference waveguides for TE and TM polarizations in the same wavelength range. The results confirm that for TE polarization, there is only ∼3 dB power difference between the integrated and reference waveguides, i.e., ∼1.5 dB loss per mode-converting tapers. Similar coupling loss values have been reported in the past [32]. The measurements for the TM input polarization (when numerically averaged over the 10-nm wavelength range) result in an average of ∼0.5 dB higher loss compared to the TE measurement. This result is qualitatively consistent with the simulated lower coupling efficiency of ∼90% for the TM mode.

4.2 Nonlinear Characterization

For nonlinear characterization, wavelength conversion via FWM is measured for the integrated waveguides of the chip. The setup for this experiment is depicted in Fig. 4. Two tunable single-mode CW laser sources (Pumps 1 and 2 with spectral ranges of 1490–1630 nm and 1515–1565 nm, respectively) are used for the input. Two polarization controllers are connected at the output of the laser sources in order to make the polarizations collinear. Both laser signals are amplified using erbium-doped fiber amplifiers (EDFAs) and then combined in a 3-dB coupler. End-butt coupling with lensed fibers is used to couple the combined signals into and out of the waveguides. The output signal is then followed by a 99:1 splitter, where one percent goes to the power meter for monitoring the alignment and ninety-nine percent is received by an optical spectrum analyzer (OSA).

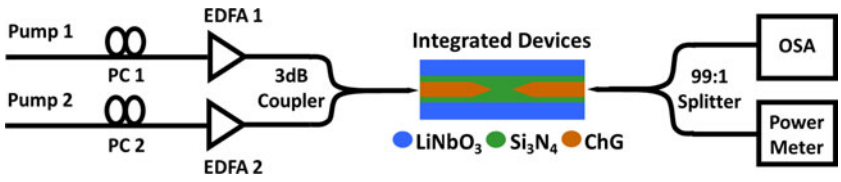

Fig. 4. Schematic of the experimental setup for wavelength conversion via FWM. PC: Polarization Controller, EDFA: Erbium-doped fiber amplifier, OSA: Optical spectrum analyzer.

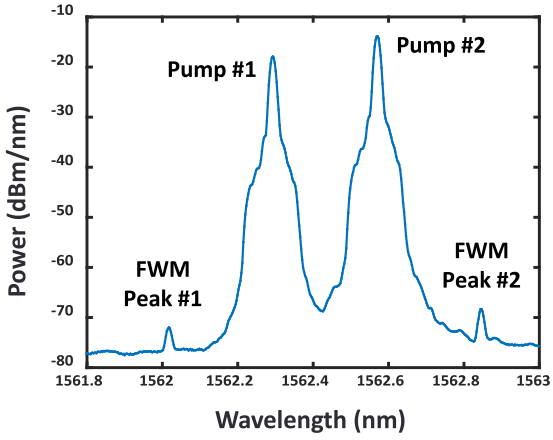

Fig. 5. Measured output spectrum from the integrated ChG-LN waveguides from the OSA at a resolution of 0.02 nm.

Both input lasers are used as pumps and idlers simultaneously, generating two FWM converted signals with higher intensity. This nonlinear experiment was performed in the integrated ChG-LN waveguides to confirm both the light coupling into ChG and the capability of the chip to generate third-order nonlinearities. The result of the experiment is shown in Fig. 5. The two higher peaks correspond to the amplified tunable lasers at 1562.29 ± 0.01 and 1562.56 ± 0.01 nm. The observed signals at the sides correspond to FWM generation at 1562.01 ± 0.01 and 1562.84 ± 0.01 nm. Although the nonlinearity in the Si_3N_4 gap may have contributed to the FWM signal, but since the length of the gap is only 1 mm, compared to 9 mm of ChG, it is expected that Si_3N_4's contribution is small, as verified by the following simulation.

Numerical study of the FWM results was performed by solving the nonlinear coupled equations [33]:

$$\frac{dA_1}{dz} = -\frac{\alpha}{2}A_1 + i\gamma\left(|A_1|^2 + 2\sum_{i\neq 1}^{4}|A_i|^2\right)A_1 + i2\gamma A_2A_3A_4^*e^{j\Delta k_1 z} + i\gamma(A_2)^2A_3^*e^{j\Delta k_2 z}, \quad (1)$$

$$\frac{dA_2}{dz} = -\frac{\alpha}{2}A_2 + i\gamma\left(|A_2|^2 + 2\sum_{i\neq 2}^{4}|A_i|^2\right)A_2 + i2\gamma\left[A_1A_4A_3^*e^{-i\Delta k_1 z} + A_1A_3A_2^*e^{-i\Delta k_2 z}\right] + i\gamma(A_3)^2A_4^*e^{j\Delta k_3 z} \quad (2)$$

$$\frac{dA_3}{dz} = -\frac{\alpha}{2}A_3 + i\gamma\left(|A_3|^2 + 2\sum_{i\neq 3}^{4}|A_i|^2\right)A_3 + i2\gamma\left[A_1A_4A_2^*e^{-i\Delta k_1 z} + A_2A_4A_3^*e^{-i\Delta k_3 z}\right] + i\gamma(A_2)^2A_1^*e^{j\Delta k_2 z} \quad (3)$$

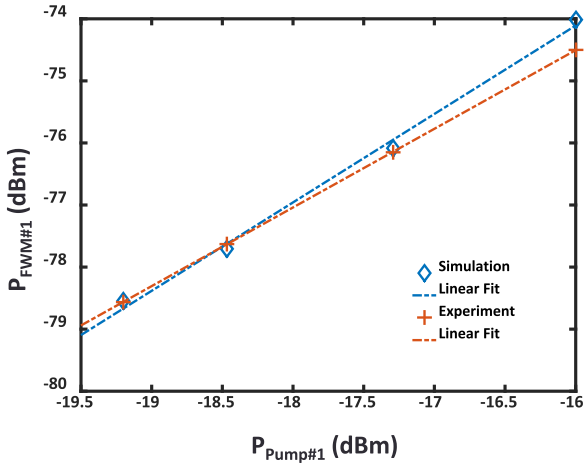

Fig. 6. Measured peak power of FWM#1 signal vs. Pump#1 power. The result is also compared with the data obtained from simulation.

$$\frac{dA_4}{dz} = -\frac{\alpha}{2}A_4 + i\gamma\left(|A_4|^2 + 2\sum_{i\neq 4}^{4}|A_i|^2\right)A_4 + i2\gamma A_2 A_3 A_1^* e^{j\Delta k_1 z} + i\gamma(A_3)^2 A_2^* e^{j\Delta k_3 z}, \tag{4}$$

where A_1, A_2, A_3, and A_4 are the field amplitudes corresponding to FWM#1, Pump#1, Pump#2 and FWM#2 in Fig. 5, respectively. α is the linear propagation loss and $\gamma = n_2\omega/cA_{eff}$ is the nonlinear parameter. These equations are obtained by solving $P^{(3)} = \frac{1}{2}\chi^{(3)}\epsilon_0 E E^* E + c.c.$ for $E = \sum_{n=1}^{4} A_n e^{j(\omega t - k_n z)}$, and considering three phase matching conditions:

$$\Delta k_1 = k_2 + k_3 - k_1 - k_4, \tag{5}$$

$$\Delta k_2 = 2k_2 - k_1 - k_3, \tag{6}$$

$$\Delta k_3 = 2k_3 - k_2 - k_4, \tag{7}$$

corresponding to the exchange of energy among the involved waves, in order to create a photon of either k_1 or k_4 wavevector.

The equations (1)–(4) are numerically solved by using Runge-Kutta-Fehlberg method for solving ordinary differential equations. The wavevectors k_n are obtained from COMSOL simulations, where the effective refractive indices of the employed waveguides were calculated. Propagation loss of 0.8 dB/cm is assumed based on our previous work on ChG waveguides with similar processing conditions [28]. An estimated γ of 15.4 $m^{-1}W^{-1}$ is assumed, according to a reported n_2 value of 3.71×10^{-18} m^2/W [25]. The coupling losses were inferred from measurements similar to those presented in Fig. 3. Fig. 6 shows the measured peak power of FWM#1 signal versus Pump#1 for different input powers with a linear fit, compared to the numerical values obtained from simulations.

It should be finally noted that the relatively low conversion efficiency of the FWM experiment is due to the discussed high coupling losses and the normal dispersion of the waveguides. Simulations on the employed waveguides suggest dispersion parameters of ~ -105 and -220 ps/(nm.km) for TE and TM modes, respectively. It is expected that if waveguides with anomalous dispersion [29] are employed higher FWM efficiency, as well as SCG can be achieved. SHG can also be potentially demonstrated by periodically polling [5] or mode-shape modulation [6] of the thin-film LN waveguides. Efforts to make these demonstrations are underway.

5. Conclusion

In summary, a heterogeneous platform is demonstrated by integrating $Ge_{23}Sb_7S_{70}$ ChG glass and Si_3N_4-LN waveguides on Si substrates. Adiabatic optical mode transition from ChG to Si_3N_4-LN is achieved through carefully designed mode-converting tapers with measured $\sim$1.5 dB loss for TE and $\sim$1.75 dB loss for TM input polarization in the 1550-nm wavelength range. Wavelength conversion via FWM is measured and compared with theory for the integrated waveguides. The straightforward and high error-tolerant fabrication process combined with the corresponding large nonlinear coefficients of LN and ChG, make this a promising platform for a variety of nonlinear optical applications. Particularly and in conjunction with reports on octave-spanning SCG [30] and SHG in thin-film LN [5], [6], the present work paves the path to demonstration of fully-integrated optical frequency combs stabilized by *f*-to-2*f* CEO locking.

Acknowledgment

The authors would like to thank P. -K. Hsu, S. Fortuna, and K. Han for assistance in ChG deposition and electron-beam lithography.

References

[1] R. Soref and J. Larenzo, "All-silicon active and passive guided-wave components for $\lambda = 1.3$ and 1.6 μm," *IEEE J. Quantum Electron.*, vol. 22, no. 6, pp. 873–879, Jun. 1986.
[2] B. Jalali and S. Fathpour, "Silicon photonics," *IEEE J. Light. Technol.*, vol. 24, no. 12, pp. 4600–4615, Dec. 2006.
[3] J. Chiles and S. Fathpour, "Silicon photonics beyond silicon-on-insulator," *J. Opt.*, vol. 19, 2017, Art. no. 053001.
[4] S. Fathpour, "Emerging heterogeneous integrated photonic platforms on silicon," *Nanophotonics*, vol. 4, no. 1, pp. 143–164, 2015.
[5] A. Rao *et al.*, "Second-harmonic generation in periodically-poled thin film lithium niobate wafer-bonded on silicon," *Opt. Exp.*, vol. 24, no. 26, pp. 29941–29947, 2016.
[6] A. Rao *et al.*, "Second-harmonic generation in single-mode integrated waveguides based on mode-shape modulation," *Appl. Phys. Lett.*, vol. 110, 2017, Art. no. 111109.
[7] X. Guo, C. L. Zou, and H. X. Tang, "Second-harmonic generation in aluminum nitride microrings with 2500%/W conversion efficiency," *Optica* vol. 3, pp. 1126–1131, 2016.
[8] W. H. P. Pernice, C. Xiong, C. Schuck, and H. X. Tang, "High-Q aluminum nitride photonic crystal nanobeam cavities," *Appl. Phys. Lett.* vol. 100, 2012, Art. no. 091105.
[9] E. Timurdogan, C. V. Poulton, M. J. Byrd, and M. R. Watts, "Electric field-induced second-order nonlinear optical effects in silicon waveguides," *Nat. Photon.*, vol. 11, pp. 200–206, 2017.
[10] M. Cazzanelli *et al.*, "Second-harmonic generation in silicon waveguides strained by silicon nitride," *Nat. Mater.*, vol. 11, pp. 148–154, 2012.
[11] A. Rao and S. Fathpour, "Second-harmonic generation in integrated photonics on silicon," *Phys. Status Solidi A*, vol. 215, no. 4, 2018, Art. no. 1700684.
[12] A. Driessen *et al.*, "Evaluation of polymer based third order nonlinear integrated optics devices," *Opt. Mater.*, vol. 9, pp. 329–333, 1998.
[13] B. Esembeson, M. L. Scimeca, T. Michinobu, F. Diederich, and I. Biaggio, "A high-optical quality supramolecular assembly for third-order integrated nonlinear optics," *Adv. Mater.*, vol. 20, no. 23, pp. 4584–4587, 2008.
[14] C. Koos *et al.*, "All-optical high-speed signal processing with siliconorganic hybrid slot waveguides," *Nat. Photon.*, vol. 3, pp. 216–219, 2009.
[15] T. J. Kippenberg, R. Holzwarth, and S. A. Diddams, "Microresonator-based optical frequency combs," *Science*, vol. 332, no. 6029, pp. 555–559, 2011.
[16] A. S. Mayer *et al.*, "Frequency comb offset detection using supercontinuum generation in silicon nitride waveguides," *Opt. Exp.*, vol. 23, no. 12, pp. 15440–15451, 2015.
[17] A. Rao *et al.*, "High-performance and linear thin-film lithium niobate Mach-Zehnder modulators on silicon up to 50 GHz," *Opt. Lett.*, vol. 41, no. 24, pp. 5700, 2016.
[18] P. Rabiei, J. Ma, S. Khan, J. Chiles, and S. Fathpour, "Heterogeneous lithium niobate photonics on silicon substrates," *Opt. Exp.*, vol. 21, no. 21, pp. 25573–25581, 2013.
[19] H. Jin *et al.*, "On-Chip generation and manipulation of entangled photons based on reconfigurable lithium-niobate waveguide circuits," *Phys. Rev. Lett.*, vol. 113, no. 24, pp. 103601, 2014.
[20] Y. -K. Jiang and A. Tomita, "The generation of polarization-entangled photon pairs using periodically poled lithium niobate waveguides in a fibre loop," *J. Phys. B: Atomic Mol. Opt. Phys.*, vol. 40, 2007, Art. no. 437.
[21] E. L. Wooten *et al.*, "A review of lithium niobate modulators for fiber-optic communications systems," *IEEE J. Quantum Electron.*, vol. 6, no. 1, pp. 69–82 Jan./Feb. 2000.
[22] J. L. Jackel, C. E. Rice, and J. J. Veselka, "Proton exchange for highindex waveguides in $LiNbO_3$," *Appl. Phys. Lett.*, vol. 41, no. 7, pp. 607–608, 1982.
[23] A. Rao *et al.*, "Heterogeneous microring and Mach-Zehnder modulators based on lithium niobate and chalcogenide glasses on silicon," *Opt. Exp.*, vol. 23, no. 17, pp. 22746–22752, 2015.

[24] L. Chang *et al.*, "Heterogeneous integration of lithium niobate and silicon nitride waveguides for wafer-scale photonic integrated circuits on silicon," *Opt. Lett.*, vol. 42, no. 4, pp. 803, 2017.
[25] J. W. Choi *et al.*, "Nonlinear characterization of GeSbS chalcogenide glass waveguides," *Sci. Rep.*, vol. 6, 2016, Art. no. 39234.
[26] K. Ikeda, R. E. Saperstein, N. Alic, and Y. Fainman, "Thermal and Kerr nonlinear properties of plasma-deposited silicon nitride/silicon dioxide waveguides," *Opt. Exp.*, vol. 16, no. 17, pp. 12987–12994, 2008.
[27] B. J. Eggleton, B. Luther-Davis, and K. Richardson, "Chalcogenide photonics," *Nat. Photon.*, vol. 5, pp. 141–148, 2011.
[28] J. Chiles, M. Malinowski, A. Rao, S. Novak, K. Richardson, and S. Fathpour, "Low-loss, submicron chalcogenide integrated photonics with chlorine plasma etching," *Appl. Phys. Lett.*, vol. 106, no. 11, 2015, Art. no. 11110.
[29] J.-E. Tremblay *et al.*, "High-Q and low-loss chalcogenide waveguide for nonlinear supercontinuum generation," in *Proc. IEEE Photon. Conf.* 2016, pp. 158–159.
[30] M. Malinowski *et al.*, "Amplified octave-spanning supercontinuum from chalcogenide waveguides for second-harmonic generation," in *Proc. IEEE Photon. Conf.* 2017, pp. 261–262.
[31] T. Barwicz and Y. Taira, "Low-cost interfacing of fibers to nanophotonic waveguides: Design for fabrication and assembly tolerances," *IEEE Photon. J.*, vol. 6, no. 4, Aug. 2014, Art. no. 6600818.
[32] T. Alto, K. Solehmainen, M. Harjanne, M. Kappulainen, and P. Heimala, "Low-loss converters between optical silicon waveguides of different sizes and types," *IEEE Photon. Tech. Lett.* vol. 18, no. 5, pp. 709–711, Mar. 2006.
[33] G. P. Agrawal, "Nonlinear Fiber Optics," 4th ed. New York, NY, USA: Academic, 2017.